***Valproic acid induces p19$^{Arf}$-mediated cellular senescence to cause neurodevelopmental defects***

Muriel Rhinn[1,2,3,4,5], Irene Zapata-Bodalo[1,2,3,4], Annabelle Klein[1,2,3,4], Jean-Luc Plassat[1,2,3,4], Tania Knauer-Meyer[1,2,3,4], and William M. Keyes[1,2,3,4,5]

[1]Institut de Génétique et de Biologie Moléculaire et Cellulaire (IGBMC), Illkirch, France.
[2]UMR7104, Centre National de la Recherche Scientifique (CNRS), Illkirch, France.
[3]U1258, Institut National de la Santé et de la Recherche Médicale (INSERM), Illkirch, France.
[4]Université de Strasbourg, Illkirch, France.

**One sentence summary:** Senescence induced by valproic acid disrupts neurodevelopment.

**Keywords**: senescence, p19$^{Arf}$, p14$^{ARF}$, neuroepithelial cell, neurogenesis, valproic acid, microcephaly, exencephaly, Cerebral organoid, Autism Spectrum Disorder, tRNA

[5] Correspondence to

Muriel Rhinn,
IGBMC,
1 Rue Laurent Fries, BP 10142,
67404 Illkirch - CU Strasbourg
France

e-mail: rhinn@igbmc.fr

Bill Keyes,
IGBMC,
1 Rue Laurent Fries, BP 10142,
67404 Illkirch - CU Strasbourg
France

bill.keyes@igbmc.fr

**Abstract**
Valproic acid (VPA) is widely prescribed to treat epilepsy, bipolar disorder and migraine. However, if taken during pregnancy, exposure to the developing embryo can cause birth defects, cognitive impairment and Autism-Spectrum Disorder. How VPA causes these developmental defects remains unclear. Here, we used embryonic mice and human organoids to model key features of drug exposure, including exencephaly, microcephaly and spinal defects. In the malformed tissues, in which neurogenesis is defective, we find that induction of cellular senescence in neuroepithelial cells is a core feature. Through genetic and functional studies, we identified $p19^{Arf}$ as the instrumental mediator of senescence and microcephaly, but not exencephaly and spinal defects. These findings identify VPA-induced ectopic senescence as a causative mechanism disrupting normal neurodevelopment, illuminating how VPA-exposure during embryonic development can lead to cognitive defects and Autism-Spectrum Disorder.

**Main Text**
Women taking VPA during pregnancy, inadequately counseled about the associated risks, have given birth to thousands of children with birth defects worldwide (*1–3*). The main associated congenital malformations include spina bifida, facial alterations and heart malformation, with additional risk of limb defects, smaller head size (microcephaly), cleft palate and more, with higher doses associated with increased risk (*1–3*). However, emerging as the most widespread consequences of VPA exposure are cognitive impairment and Autism Spectrum Disorder (ASD), which occur in 30-40% of exposed infants, and which can occur without any major physical deformity (*1*, *4–6*). The connection between VPA exposure and birth defects has been validated in rodent and primate models, leading to the hypothesis that cognitive defects arise from disruption of early neurodevelopment, around the stage of neural tube closure (*6–9*). The molecular mechanisms by which VPA perturbs development are mostly unknown, but likely result from its function as a histone-deacetylase inhibitor (HDACi) (*10*). In this capacity, VPA is broadly used in cancer therapy, and is known to induce cellular senescence (*11*). As a response mechanism to tissue damage and cellular stress, senescence is a state of permanent cell cycle arrest, mediated by tumor-suppressor genes such as $p16^{Ink4a}$, $p19^{Arf}$ ($p14^{Arf}$ in humans), *p53* and *p21*, that are also susceptible to induction by HDACi's (*11–13*). While timely activation of senescence can be beneficial during development and wound-healing, mis-timed or chronic senescence can be detrimental (*14–19*). Given these relationships, we investigated whether VPA might cause developmental defects in part through senescence induction.

Drawing from earlier VPA-exposure studies in mice (*8*, *20*), we established a time-course paradigm for assessing acute and developmental phenotypes caused by VPA during embryonic development (see experimental scheme Fig S1A). We first analyzed E13.5 embryos from pregnant female mice that had been dosed three times around E8. In intact embryos, we identified prominent and recurrent defects, such as exencephaly (a condition where the brain is located outside of the skull), a small brain (microcephaly) (Fig. 1A), and spinal cord curvature (not shown). Although in humans VPA causes spina bifida, a posterior neural tube closure defect where part of the spinal cord and nerves are exposed, in mice, this results in exencephaly, a defect of anterior neural tube closure (*21*). Next, we analyzed VPA-exposed embryos at earlier developmental stages, and could visually distinguish all phenotypes at E10.5, and even as early as E9.5, where they presented as an open neural tube and/or a smaller brain (referred to as microcephaly from here on), and gross misalignment of the neural tube and somites (Figs. 1A and S1B). Our analyses demonstrate that VPA can cause early and distinct phenotypic changes during early mouse brain development that recapitulate features of VPA-exposure in humans.

To investigate how such early exposure to VPA impacted on cortical development, we analyzed telencephalic corticogenesis at later developmental stages. When we performed

immunostaining in microcephalic embryos for the neural progenitor markers Pax6 (apical progenitors), and Tbr2 (intermediate progenitors), and for the neuronal differentiation marker Tuj1, we found a significant decrease in progenitors and neurons at E10.5 in VPA-exposed embryos (Fig. S2) and E13.5. (Fig. 1B). Similar results were seen in exencephalic embryos (not shown), demonstrating that one effect of VPA is decreased neurogenesis. Overall, these data validate that VPA-exposure in pregnant mice model embryonic neurodevelopmental birth defects.

Next, we investigated whether cellular senescence was a feature in VPA-exposed mouse embryos. First, we performed wholemount staining to detect any activity of the senescence marker beta-galactosidase (SA-β-gal) on E9.5 control or VPA-exposed embryos presenting with exencephaly or microcephaly. We found that ectopic SA-β-gal activity was prominent in the forebrain and hindbrain in both exencephalic and microcephalic embryos (Fig. 2A). Unexpectedly, this ectopic staining was absent in both the spinal cord and somites. In sectioned embryos however, we found that SA-β-gal activity was prominent in the neuroepithelial cells, the embryonic precursors of neurons and glia in the brain (Fig. 2B). Upon assessing EdU incorporation, we confirmed that neuroepithelial cells were proliferative in control but not in VPA-exposed embryonic mice (Fig. 2C). In addition, while apoptotic cells were present on the surface ectoderm of the VPA-exposed embryos, as assessed by wholemount TUNEL staining, we did not detect any cell death in the neuroepithelial cells (Fig S3). We then dissected the forebrain and midbrain regions from wildtype or VPA-exposed microcephalic embryos at E8.75 and performed quantitative real-time PCR (qRT-PCR) for senescence genes, including cell cycle inhibitors and secreted components of the senescence-associated secretory phenotype (SASP). We found that *p21*, $p19^{Arf}$ and $p16^{Ink4a}$ and the SASP genes *IL6*, *IL1a*, *IL1b*, *Pai1* were strongly induced in VPA-exposed embryos (Fig 2D). Together, these data uncover that VPA induces ectopic senescence in neuroepithelial cells during developmental neurogenesis.

We next sought to assess if VPA exposure might similarly induce senescence in human neuroepithelial cells, and used cerebral organoids to investigate this possibility. We grew organoids as previously described (*22*), and exposed these to different concentrations of VPA at time points equivalent to developmental stages in mouse. Specifically, we treated cultures with 1-2mM VPA from day 18-25, and analyzed the organoids upon VPA removal at day 25, or allowed the organoids to develop until day 42, when neuronal differentiation could be assessed (Fig. 3A).

Exposure to VPA caused a significant decrease in organoid growth that persisted after drug removal (Fig. 3B). As in mice, we assessed cortical neurogenesis in VPA-treated organoids, and found a significantly reduced expression of progenitor (Pax6, Tbr2 and Sox1) and neuronal (Tuj1) markers (Fig. 3C and Fig. S4). When we assessed senescence using wholemount SA-β-gal staining, we detected a strong induction in the organoids, which upon sectioning was found to be present specifically in the neuroepithelial cells (Fig. 3D). Proliferation was also decreased in these cells, as measured by anti phospho-Histone H3 (PHH3) staining (Fig. 3E). Finally, we assessed expression of key senescence mediators by qRT-PCR at day 25. Interestingly, we observed a significant induction of $p14^{ARF}$ (human ortholog of $p19^{Arf}$), and the SASP genes *IL1a* and *Pai1*, but no change in $p16^{IINK4A}$ or *p21* expression (Fig. 3F).

Thus far, our experiment uncovered that exposure to VPA causes a pronounced induction of senescence in neuroepithelial cells that is associated with a marked decrease in proliferation and neurogenesis. To investigate if senescence arrest is functionally coupled to VPA-induced phenotypes and impaired neurogenesis, we employed genetic loss of function models. When we treated pregnant mice deficient for the senescence genes *p21*, $p19^{Arf}$ or $p16^{Ink4a}$ with VPA, and assessed E9.5 embryos, we found that *p21*- and $p16^{Ink4a}$ -deficient embryos had no visible improvement in phenotype and even had a slight increase in exencephaly relative to wildtype mice (Fig. 4A and Fig. S5). However, although embryos deficient in $p19^{Arf}$ and exposed to VPA

displayed no change in exencephaly or spinal curvature defects relative to wildtype mice, they were otherwise noticeably improved, as evidenced by a reduction in the incidence and/or severity of microcephaly (Fig. 4A). To validate our observations, we measured the combined forebrain and midbrain area in these embryos. At this early stage (one day after VPA exposure), we found that the forebrain/midbrain size in *p19$^{Arf}$*-deficient embryos was significantly larger compared to wildtype VPA-exposed embryos (Fig. 4B). The lessened size reduction was also evident with *in situ* hybridization for the forebrain marker *Six3* (Fig. S6). To assess whether the size difference phenotype correlated with changes in senescence, we again assessed SA-β-gal staining, and found that VPA-exposed *p19$^{Arf}$*-deficient mice had reduced expression in the neuroepithelial cells relative to VPA-exposed wildtype embryos (Fig. 4C). Furthermore, when assessed by qRT-PCR, *p19$^{Arf}$*-deficiency was associated with a decrease in *p16$^{Ink4a}$* and a reduced SASP-response (Fig. S7). In agreement with the results from human organoids, this data point to *p19$^{Arf}$* functioning as a mediator of VPA-induced senescence in the embryo.

Given that *p19$^{Arf}$*-deficiency is protective for VPA-induced embryonic developmental defects, we wanted to understand the underlying mechanism at a molecular level. To this end, we performed RNA-sequencing on the forebrain/midbrain region from both wildtype and *p19$^{Arf}$*-deficient embryos, either treated or untreated with VPA. Through phenotype pathway analysis of differentially expressed genes it was evident that many neurodevelopmental and ASD-related phenotypes, including exencephaly and microcephaly, were associated with significantly downregulated genes in VPA-exposed wildtype mice. Specifically, these gene signatures were associated with Wnt and Hippo signaling (*23*) (Fig. 4D and Fig. S8A). In *p19$^{Arf}$*-deficient animals however, most of these signatures were significantly less affected, confirming our phenotypic observations of the genetic backgrounds (Fig. 4D and Fig. S8A).

Genetic population studies have identified candidate genes associated with microcephaly and ASD (*24*, *25*). Many of these genes are significantly decreased in both the forebrain and midbrain of VPA-exposed wildtype embryos, including Chd8, Dyrk1a, Fmr1, Cep63, and others. However, most were not restored upon *p19$^{Arf}$*-loss (Fig. S8 B,C), suggesting that senescence may be regulated independently beyond these specific genes. Therefore, to get a better understanding of how p19$^{Arf}$ might induce these ectopic phenotypes, we analyzed the subset of genes that were significantly downregulated in VPA-exposed wildtype embryos, but that were not significantly decreased in *p19$^{Arf}$* -deficient embryos (red genes in Fig 4E). Within this p19$^{Arf}$-dependent gene set, we identified tRNA aminoacylation and tRNA export (Fig. 4F and Fig. S8D). Interestingly, perturbation of tRNAs or their regulatory mechanisms is linked to microcephaly and neurodevelopmental defects (*26*). This suggests that p19$^{Arf}$-mediated senescence and repression of these genes may contribute to microcephaly and cognitive impairment.

To investigate if ectopic p19$^{Arf}$ expression is sufficient to induce senescence and developmental defects when expressed in the neuroepithelium, we electroporated mouse *p19$^{Arf}$* into the neuroepithelial cells of chick embryo forebrains. In comparison to GFP-control plasmid, we found that *p19$^{Arf}$* expression caused a unilateral perturbation of development, decreasing forebrain size, and induced strong ectopic SA-β-gal activity in the neuroepithelial cells (Fig. 4G and Fig. S9). These data demonstrate that aberrant *p19$^{Arf}$* expression is sufficient to induce senescence and developmental defects. Finally, we asked whether p19$^{Arf}$ deficiency in and of itself would rescue some of the major defects caused by VPA exposure. To answer this question, we measured progenitor and neuronal status during cortical neurogenesis at later stages, when neurodevelopment has progressed further. As before, wildtype embryos exposed to VPA and examined at E13.5 presented with a significant reduction in the number of progenitors and neurons (Fig. 4H). Strikingly however, *p19$^{Arf}$*-deficient mice were not as susceptible to VPA exposure, and presented with significantly increased numbers of progenitors, as well as increased thickness of the neuronal zone relative to wildtype embryos.

These experiments demonstrate that $p19^{Arf}$, in response to VPA, drives a senescence-mediated block in neurogenesis.

## Discussion

Together, these findings advance our understanding of how VPA causes neurodevelopmental defects, identifying $p19^{Arf}$-mediated senescence as a key contributing mechanism. Interestingly, this does not appear to be mechanistically linked with the exencephaly and spinal defects caused by the drug. Instead, senescence disrupts neurogenesis, which in this high-dose model leads to microcephaly. Our data suggest that induction of ectopic senescence by VPA during early development contributes to the resulting cognitive defects including ASD, in a manner that appears separate from the main congenital malformations caused by the drug.

Furthermore, although VPA is an HDACi, which is a class associated with gene-activation, we find, as did others, that the developmental phenotypes are associated with down-regulated and not up-regulated genes (*25*). Among these, we identify tRNA regulation as one of the most significantly restored pathways in the absence of $p19^{Arf}$. Importantly, $p19^{Arf}$ can directly block tRNA synthesis (*27*), while disruption of tRNA function is strongly associated with microcephaly and neurodevelopmental disorders (*26*, *28–32*). Together, our findings support that VPA induction of $p19^{Arf}$-mediated senescence causes a broad repression of key developmental pathways, including tRNA function, thereby disrupting early neurodevelopmental steps.

Finally, this works makes an unexpected functional connection between aberrant senescence and developmental defects. Our discovery that atypical activation of senescence in the embryo can perturb development raises the intriguing possibility that it may also contribute to defects in developmental contexts beyond those we studied here.

## Materials and Methods

*Animal maintenance and VPA administration*

Pregnant CD1, C57Bl6/J, p21-/-, $p19^{Arf}$-/- and $p16^{Ink4a}$ -/- were maintained in a temperature- and humidity-controlled animal facility with a 12h light/dark cycle. We administrated 400mg/kg (Sigma-aldrich) VPA or PBS as control, intra-peritoneally to timed-pregnant females, at embryonic day (ED) 8 (3 times (9am, 1pm, 4pm). The p21-/-, $p19^{Arf}$-/- and $p16^{Ink4a}$ -/- mice were on a C57BL6J background, so were compared to C57BL6J wildtype as control. We observed that the C57Bl6J mice are more sensitive than the CD1 mice to induction of microcephaly (Fig. 1A and Fig. 4A). For qRT-PCR and RNA-seq analysis, only the first 2 doses were administered, and samples were collected at E8.75. All the experimental procedures were in full compliance with the institutional guidelines of the accredited IGBMC/ICS animal house, in compliance with French and EU regulations on the use of laboratory animals for research, under the supervision of Dr. Bill Keyes who holds animal experimentation authorizations from the French Ministry of Agriculture and Fisheries (#12840).

*Organoids*

Cerebral organoids were generated from the iPSC line HPSI0214i-kucg_2 (Catalog# 77650065, HipSci) using the STEMdiff™ Cerebral Organoid Kit (Catalog #08570 and #08571) from StemCell Technologies. Representative pictures were acquired with a LEICA DMS 1000. We acknowledge Wellcome Trust Sanger Institute as the source of HPSI0214i-kucg_2 human induced pluripotent cell line which was generated under the Human Induced Pluripotent Stem Cell Initiative funded by a grant from the Wellcome Trust and Medical Research Council, supported by the Wellcome Trust (WT098051) and the NIHR/Wellcome Trust Clinical Research Facility, and acknowledges Life Science Technologies Corporation as the provider of “Cytotune.”

*Immunofluorescence*

Embryos and organoids were fixed in 4% PFA for 30 min at 4°C, washed in PBS, and processed for paraffin embedding. Sections were obtained using a microtome (8 µm, Leica 2035 Biocut). After antigen unmasking in citrate buffer (0.01 M, pH 6) for 15 min in a microwave oven, slides were blocked with 5% donkey serum, 0.1% TritonX-100 in phosphate-buffered saline (PBS) and incubated overnight with the following primary antibodies: phospho-histone H3 (1:500, Upstate #05-806); Pax6 (1:300, Covance #PRB-278P); Tbr2 (1:300, eBioscience #14-4875); Sox1 (1:50, R&D systems #AF3369); βIII-tubulin/Tuj1 (1:200, Covance #MMS-435P-100); p19$^{Arf}$ (5-C3-1) rat monoclonal antibody (Santa-Cruz #sc-32748); GFP 2A3 (IGBMC). Primary antibodies were visualized by immunofluorescence using secondary antibodies from donkey (1:400, Invitrogen: Alexa Fluor 568 donkey anti-mouse IgG #A-100037, Alexa Fluor 488 donkey anti-rat IgG #A-21208, Alexa Fluor 488 donkey anti-rabbit #A-21206, Alexa Fluor 568 donkey anti-Goat IgG #A-11057) and from goat (1:400, Invitrogen: Alexa Fluor 568 goat anti-rabbit IgG #A-110111,Alexa Fluor 488 goat anti-mouse IgG #A11001, Alexa Fluor 568 anti-rat IgG #A11077), and cell nuclei were identified using DAPI (1:2000). Stained sections were digitized using a slide scanner (Nanozoomer 2.0-HT, Hamamatsu, Japan), and measurements (thickness of the neuronal layer) were performed using the NDPview software of the digital scanner.

*SA-ß-gal staining*

Whole-mount SA-ß-gal, was detected as previously described (Storer et al., 2013). Incubation with X-gal was performed overnight for mouse embryos and 1h30 for organoids. For determination of specific localization of senescence in embryonic tissue, embryos stained with SA-ß-gal were post-fixed in 4% PFA overnight at 4°C, embedded in paraffin and sectioned. Representative pictures were acquired using a macroscope (Leica M420) and stained sections were digitized using a slide scanner (Nanozoomer 2.0-HT, Hamamatsu, Japan)

*EdU*

To assess cell proliferation in embryos, pregnant female mice at E9.5 were injected intraperitoneally with 5-ethynyl-2´-deoxyuridine (EdU; 50 mg/kg body weight) for 1 hr. Click-iT® EdU Alexa Fluor® 488 Imaging Kit (Thermofisher) was used as per manufacturers protocol. Representative pictures were acquired using a microscope (DM4000B).

*TUNEL*

Cell death was assessed using the TdT-mediated dUTP nick end-labeling (TUNEL) method (ApopTagPeroxidase In Situ Apoptosis detection kit, Millipore) as per manufacturers' instructions. Representative pictures were acquired using a macroscope (Leica M420) and a microscope (DM4000B).

*RT-qPCR and analysis*

The combined forebrain and midbrain region was manually dissected from E8.75 embryos, and snap-frozen. RNA was extracted from individual embryos using the RNAeasy mini kit (Qiagen). 10 ng RNA were used for analysis with the LUNA one-step RT-qPCR kit (LUNA E3005L Biolabs). The relative expression levels of the mRNA of interest were determined by real-time PCR using Quantifast SYBR Green Mix (Qiagen) with specific primers listed in Supplementary Table 1 and a LightCycler 480 (Roche). Samples were run in triplicate and gene of interest expression was normalized to human Gapdh or mouse Rplp0.

*In ovo electroporation*

Fertilized chicken embryos were obtained from local farmers. Chick eggs were incubated in a humidified chamber at 37°C, and embryos were staged according to (Hamburger and Hamilton, 1951). 1.5 µg/µL DNA constructs (pCAGGS-GFP [a gift from Dr J. Godin, IGBMC] or pCAGGS-p19$^{ARF}$-GFP [p19$^{Arf}$ coding sequence was cloned in XhoI/NheI multiple cloning sites in the pCAGGS-GFP]) mixed with 0.05% Fast Green (Sigma) were injected into neural tubes of stage HH8 chick embryos and electroporated on the right side, leaving the left side as untreated control. Electroporation was performed using a square wave electroporator (BTX

ECM 830 electroporation system) and the parameters applied: three pulses of 15V for 30ms with an interval of 1s. Embryos were harvested 24 hours after electroporation and processed for SA-ß-gal, histology and immunohistochemistry. Representative pictures were acquired using a macroscope (Leica Z16 APO) and a microscope (Leica DM4000B).

*Whole-mount in situ hybridization.*
RNA probes were prepared by *in vitro* transcription using the Digoxigenin-RNA labeling mix (Roche). Template plasmids were kindly provided by Drs G. Oliver (*Six3*) and S.L. Ang (*Mox1*). Mouse embryos were dissected in ice-cold PBS and fixed O/N in 4% paraformaldehyde (PFA)/PBS. After several washes in PBS1X/0.1% Tween-20 (PBT), embryos were bleached for 1 h in 3% $H_2O_2$/PBT and washed in PBT before being digested with Proteinase K (10mg/ml) for 2min. Digestion was stopped by 5 min incubation in 2 mg/ml glycine/ PBT. Embryos were washed again in PBT before post-fixing for 20 min in 0.2% glutaraldehyde/4% PFA/PBS. After further washes they were incubated in prewarmed hybridization buffer (50% deionized formamide, 5XSSC, 1%SDS, 100µg/ml tRNA) and prehybridized for 2 h at 65 °C. The buffer was then replaced with fresh prewarmed hybridization buffer containing the digoxigenin labeled RNA probes and incubated O/N at 65 °C. The next day, embryos were washed twice in buffer 1 (50% formamide; 5XSSC; 1%SDS) at 65 °C then in buffer 2 (NaCl 500mM, 10mM TrisHCl pH=7.5, 0.1%Tween20) at room temperature before treating them with RNaseA (100mg/ml) to reduce background. The embryos were rinsed in buffer 2, then in buffer 3 (50% formamide, 2XSSC). Finally, the embryos are rinsed in TBS/0.1% Tween-20 (TBST) then blocked for 2 h in 2% blocking solution (Roche) and incubated O/N in the same solution containing 1:2,500 anti-digoxigenin antibody (Roche). The next day the embryos were washed in TBST, before washing them in NTMT (NaCl 100mM, Tris-HCl 100mM pH=9,5, $MgCl_2$ 50mM, Tween20 at 0.1%) and developing the signal in the dark with staining solution (4.5 µl/ml NBT and 3.5 µl/ml BCIP (Roche) in NTMT buffer).

*RNA sequencing*
RNA was collected as for qRT-PCR. Full length cDNA was generated from 10 ng of total RNA from 4 individual embryos per treatment, using Clontech SMART-Seq v4 Ultra Low Input RNA kit for Sequencing (Takara Bio Europe, Saint Germain en Laye, France) according to manufacturer's instructions with 8 cycles of PCR for cDNA amplification by Seq-Amp polymerase. Six hundred pg of pre-amplified cDNA were then used as input for Tn5 transposon tagmentation by the Nextera XT DNA Library Preparation Kit (96 samples) (Illumina, San Diego, CA) followed by 12 cycles of library amplification. Following purification with Agencourt AMPure XP beads (Beckman-Coulter, Villepinte, France), the size and concentration of libraries were assessed by capillary electrophoresis using the Agilent 2100 Bioanalyzer.

Sequencing was performed on an Illumina HiSeq 4000 in a 1x50bp single end format. Reads were preprocessed using cutadapt 1.10 in order to remove adaptors and low-quality sequences, and reads shorter than 40 bp were removed from further analysis. Remaining reads were mapped to Homo sapiens rRNA sequences using bowtie 2.2.8, and reads mapped to those sequences were removed from further analysis. Remaining reads were aligned to mm10 assembly of Mus musculus with STAR 2.5.3a. Gene quantification was performed with htseq-count 0.6.1p1, using “union” mode and Ensembl 101 annotations. Differential gene expression analysis was performed using DESeq2 1.16.1 Bioconductor R package on previously obtained counts (with default options). P-values were adjusted for multiple testing using the Benjamini and Hochberg method. Adjusted p-value <0.05 was taken as statistically significant.

Pathway analysis was performed using Enrichr (http://amp.pharm.mssm.edu/Enrichr.) with Gene Ontology 2018 and MGI Mammalian Phenotype Level 4 2019 databases. Adjusted p-value of <0.25 was used as a threshold to select the significant enrichment. The sequencing data have been uploaded to the Gene Expression Omnibus (GEO) database with accession number pending.

*Counting and Statistical analysis*
For cell number quantification, positive cells for a given marker (Pax6, Tbr2 or Tuj1) were counted in a 100μm width columnar area from the ventricular zone to the apical surface in similar regions in the cortex. Immunofluorescence analyses, area measurements, and RNA expression were statistically analyzed using Prism (GraphPad, San Diego, California, United States). At least five animals of each treatment from three different litters were analyzed. Cell counting was performed on three adjacent sections. Results are presented as mean ± S.E.M. Statistical analysis was carried out employing the Mann-Whitney test for unpaired variables. For 3 or more groups, normal multiple comparisons were tested with one-way ANOVA plus Tukey post-hoc test and non-normal multiple comparisons were tested using Kruskal–Wallis test followed by a Dunn's test. P-values < 0.05 were considered significant ( *p ≤ 0.05, **p ≤ 0.01, ***p ≤ 0.001 and ****p ≤ 0.0001).

**Acknowledgements**
We thank Travis Stracker, Juliette Godin, Michele Studer, Pura Munoz, Birgit Ritschka, Christina Lilliehook (Life Science Editors) and members of the Keyes lab for comments on the manuscript. We thank the core facilities at the IGBMC for excellent technical support, including the Sequencing, Cell Culture and Microscopy platforms, the mouse facilities of the IGBMC and the Mouse Clinical Institute (ICS), and in particular Sylvie Falcone, Amélie Freismuth, Marion Humbert, Jean-Marie Garnier and Olivia Wendling for technical assistance. Sequencing was performed by the GenomEast platform, a member of the "France Génomique" consortium (ANR-10-INBS-0009). Work in the Keyes lab was funded in part by grants from: La Fondation Recherche Medicale (FRM) (AJE20160635985), Fondation ARC (PJA20181208104), IDEX Attractivité - University of Strasbourg (IDEX2017), La Fondation Schlumberger pour l'Education et la Recherche FSER 19 (Year 2018)/FRM, ANR (ANR-19-CE13-0023-03) and La Ligue Contre le Cancer. Work was also supported by the grant ANR-10-LABX-0030-INRT, a French State fund managed by the Agence Nationale de la Recherche under the frame program Investissements d'Avenir ANR-10-IDEX-0002-02.

**References**

1. J. Clayton-Smith, R. Bromley, J. Dean, H. Journel, S. Odent, A. Wood, J. Williams, V. Cuthbert, L. Hackett, N. Aslam, H. Malm, G. James, L. Westbom, R. Day, E. Ladusans, A. Jackson, I. Bruce, R. Walker, S. Sidhu, C. Dyer, J. Ashworth, D. Hindley, G. A. Diaz, M. Rawson, P. Turnpenny, Diagnosis and management of individuals with Fetal Valproate Spectrum Disorder; a consensus statement from the European Reference Network for Congenital Malformations and Intellectual Disability. *Orphanet J. Rare Dis.* **14**, 1–21 (2019).
2. J. Jentink, M. A. Loane, H. Dolk, I. Barisic, E. Garne, J. K. Morris, L. T. W. D. J. Van Den Berg, Valproic acid monotherapy in pregnancy and major congenital malformations. *N. Engl. J. Med.* **362**, 2185–93 (2010).
3. A. V. Margulis, S. Hernandez-Diaz, T. McElrath, K. J. Rothman, E. Plana, C. Almqvist, B. M. D'Onofrio, A. S. Oberg, Relation of in-utero exposure to antiepileptic drugs to pregnancy duration and size at birth. *PLoS One*. **14**, e0214180 (2019).
4. K. J. Meador, G. A. Baker, N. Browning, M. J. Cohen, R. L. Bromley, J. Clayton-Smith, L. A. Kalayjian, A. Kanner, J. D. Liporace, P. B. Pennell, M. Privitera, D. W. Loring, Fetal antiepileptic drug exposure and cognitive outcomes at age 6 years (NEAD study): A prospective observational study. *Lancet Neurol.* **12**, 244–252 (2013).
5. Mogens Vestergaard Jakob Christensen, ; Therese Koops Grønborg, ; Merete Juul Sørensen, ; Diana Schendel, ; Erik Thorlund Parner, ; Lars Henning Pedersen, Prenatal valproate exposure and risk of autism spectrum disorders and childhood autism. *JAMA*. **309**, 1696–1703 (2013).
6. F. I. Roullet, J. K. Y. Lai, J. A. Foster, In utero exposure to valproic acid and autism - A

current review of clinical and animal studies. *Neurotoxicol. Teratol.* **36**, 47–56 (2013).
7. M. Varghese, N. Keshav, S. Jacot-Descombes, T. Warda, B. Wicinski, D. L. Dickstein, H. Harony-Nicolas, S. De Rubeis, E. Drapeau, J. D. Buxbaum, P. R. Hof, Autism spectrum disorder: neuropathology and animal models. *Acta Neuropathol.* **134**, 537–566 (2017).
8. C. Nicolini, M. Fahnestock, The valproic acid-induced rodent model of autism. *Exp. Neurol.* **299**, 217–227 (2018).
9. H. Zhao, Q. Wang, T. Yan, Y. Zhang, H. juan Xu, H. peng Yu, Z. Tu, X. Guo, Y. hui Jiang, X. jiang Li, H. Zhou, Y. Q. Zhang, Maternal valproic acid exposure leads to neurogenesis defects and autism-like behaviors in non-human primates. *Transl. Psychiatry*. **9**, 1–13 (2019).
10. R. X. Moldrich, G. Leanage, D. She, E. Dolan-Evans, M. Nelson, N. Reza, D. C. Reutens, Inhibition of histone deacetylase in utero causes sociability deficits in postnatal mice. *Behav. Brain Res.* **257**, 253–264 (2013).
11. X. N. Li, Q. Shu, J. M. F. Su, L. Perlaky, S. M. Blaney, C. C. Lau, Valproic acid induces growth arrest, apoptosis, and senescence in medulloblastomas by increasing histone hyperacetylation and regulating expression of p21Cip1, CDK4, and CMYC. *Mol. Cancer Ther.* **4**, 1912–1922 (2005).
12. A. Matheu, P. Klatt, M. Serrano, Regulation of the INK4a/ARF locus by histone deacetylase inhibitors. *J. Biol. Chem.* **280**, 42433–42441 (2005).
13. R. Soriano-Cantón, A. Perez-Villalba, J. M. Morante-Redolat, M. Á. Marqués-Torrejón, M. Pallás, F. Pérez-Sánchez, I. Fariñas, Regulation of the p19Arf/p53 pathway by histone acetylation underlies neural stem cell behavior in senescence-prone SAMP8 mice. *Aging Cell*. **14**, 453–462 (2015).
14. B. Ritschka, M. Storer, A. Mas, F. Heinzmann, M. C. Ortells, J. P. Morton, O. J. Sansom, L. Zender, W. M. Keyes, The senescence-associated secretory phenotype induces cellular plasticity and tissue regeneration. *Genes Dev.* **31**, 172–183 (2017).
15. D. Muñoz-Espín, M. Cañamero, A. Maraver, G. Gómez-López, J. Contreras, S. Murillo-Cuesta, A. Rodríguez-Baeza, I. Varela-Nieto, J. Ruberte, M. Collado, M. Serrano, Programmed cell senescence during mammalian embryonic development. *Cell*. **155**, 1104 (2013).
16. M. Rhinn, B. Ritschka, W. M. Keyes, Cellular senescence in development, regeneration and disease. *Dev.* **146**, 1–10 (2019).
17. M. Demaria, N. Ohtani, S. A. Youssef, F. Rodier, W. Toussaint, J. R. Mitchell, R. M. Laberge, J. Vijg, H. VanSteeg, M. E. T. Dollé, J. H. J. Hoeijmakers, A. deBruin, E. Hara, J. Campisi, An essential role for senescent cells in optimal wound healing through secretion of PDGF-AA. *Dev. Cell*. **31**, 722–733 (2014).
18. D. Muñoz-Espín, M. Serrano, Cellular senescence: From physiology to pathology. *Nat. Rev. Mol. Cell Biol.* **15**, 482–496 (2014).
19. M. Storer, A. Mas, A. Robert-Moreno, M. Pecoraro, M. C. Ortells, V. Di Giacomo, R. Yosef, N. Pilpel, V. Krizhanovsky, J. Sharpe, W. M. Keyes, Senescence is a developmental mechanism that contributes to embryonic growth and patterning. *Cell*. **155** (2013).
20. K. Ehlers, H. Sturje, H. J. Merker, H. Nau, Vaproic acid-induced spina bifida: a mouse model. *Teratology*. **45**, 145–154 (1992).
21. H. Nau, R. -S Hauck, K. Ehlers, Valproic Acid-Induced Neural Tube Defects in Mouse and Human: Aspects of Chirality, Alternative Drug Development, Pharmacokinetics and Possible Mechanisms. *Pharmacol. Toxicol.* **69**, 310–321 (1991).
22. M. A. Lancaster, M. Renner, C. A. Martin, D. Wenzel, L. S. Bicknell, M. E. Hurles, T. Homfray, J. M. Penninger, A. P. Jackson, J. A. Knoblich, Cerebral organoids model human brain development and microcephaly. *Nature*. **501**, 373–379 (2013).
23. V. Kwan, B. K. Unda, K. K. Singh, Wnt signaling networks in autism spectrum disorder and intellectual disability. *J. Neurodev. Disord.* **8**, 1–10 (2016).
24. D. Jayaraman, B. Il Bae, C. A. Walsh, The genetics of primary microcephaly. *Annu. Rev. Genomics Hum. Genet.* **19**, 177–200 (2018).

25. A. Takata, N. Miyake, Y. Tsurusaki, R. Fukai, S. Miyatake, E. Koshimizu, I. Kushima, T. Okada, M. Morikawa, Y. Uno, K. Ishizuka, K. Nakamura, M. Tsujii, T. Yoshikawa, T. Toyota, N. Okamoto, Y. Hiraki, R. Hashimoto, Y. Yasuda, S. Saitoh, K. Ohashi, Y. Sakai, S. Ohga, T. Hara, M. Kato, K. Nakamura, A. Ito, C. Seiwa, E. Shirahata, H. Osaka, A. Matsumoto, S. Takeshita, J. Tohyama, T. Saikusa, T. Matsuishi, T. Nakamura, T. Tsuboi, T. Kato, T. Suzuki, H. Saitsu, M. Nakashima, T. Mizuguchi, F. Tanaka, N. Mori, N. Ozaki, N. Matsumoto, Integrative Analyses of De Novo Mutations Provide Deeper Biological Insights into Autism Spectrum Disorder. *Cell Rep.* **22**, 734–747 (2018).
26. A. E. Schaffer, O. Pinkard, J. M. Coller, TRNA Metabolism and Neurodevelopmental Disorders. *Annu. Rev. Genomics Hum. Genet.* **20**, 359–387 (2019).
27. J. P. Morton, T. Kantidakis, R. J. White, RNA polymerase III transcription is repressed in response to the tumour suppressor ARF. *Nucleic Acids Res.* **35**, 3046–3052 (2007).
28. L. Wang, Z. Li, D. Sievert, D. E. C. Smith, M. I. Mendes, D. Y. Chen, V. Stanley, S. Ghosh, Y. Wang, M. Kara, A. D. Aslanger, R. O. Rosti, H. Houlden, G. S. Salomons, J. G. Gleeson, Loss of NARS1 impairs progenitor proliferation in cortical brain organoids and leads to microcephaly. *Nat. Commun.* **11**, 1–12 (2020).
29. M. L. Hoye, D. L. Silver, Decoding mixed messages in the developing cortex: translational regulation of neural progenitor fate. *Curr. Opin. Neurobiol.* **66**, 93–102 (2021).
30. M. E. Kuo, A. F. Theil, A. Kievit, M. C. Malicdan, W. J. Introne, T. Christian, F. W. Verheijen, D. E. C. Smith, M. I. Mendes, L. Hussaarts-Odijk, E. van der Meijden, M. van Slegtenhorst, M. Wilke, W. Vermeulen, A. Raams, C. Groden, S. Shimada, R. Meyer-Schuman, Y. M. Hou, W. A. Gahl, A. Antonellis, G. S. Salomons, G. M. S. Mancini, Cysteinyl-tRNA Synthetase Mutations Cause a Multi-System, Recessive Disease That Includes Microcephaly, Developmental Delay, and Brittle Hair and Nails. *Am. J. Hum. Genet.* **104**, 520–529 (2019).
31. X. Zhang, J. Ling, G. Barcia, L. Jing, J. Wu, B. J. Barry, G. H. Mochida, R. S. Hill, J. M. Weimer, Q. Stein, A. Poduri, J. N. Partlow, D. Ville, O. Dulac, T. W. Yu, A. T. N. Lam, S. Servattalab, J. Rodriguez, N. Boddaert, A. Munnich, L. Colleaux, L. I. Zon, D. Söll, C. A. Walsh, R. Nabbout, Mutations in QARS, encoding glutaminyl-trna synthetase, cause progressive microcephaly, cerebral-cerebellar atrophy, and intractable seizures. *Am. J. Hum. Genet.* **94**, 547–558 (2014).
32. S. Blanco, S. Dietmann, J. V Flores, S. Hussain, C. Kutter, P. Humphreys, M. Lukk, P. Lombard, L. Treps, M. Popis, S. Kellner, S. M. Hölter, L. Garrett, W. Wurst, L. Becker, T. Klopstock, H. Fuchs, V. Gailus-Durner, M. Hrabě de Angelis, R. T. Káradóttir, M. Helm, J. Ule, J. G. Gleeson, D. T. Odom, M. Frye, Aberrant methylation of tRNAs links cellular stress to neuro-developmental disorders . *EMBO J.* **33**, 2020–2039 (2014).

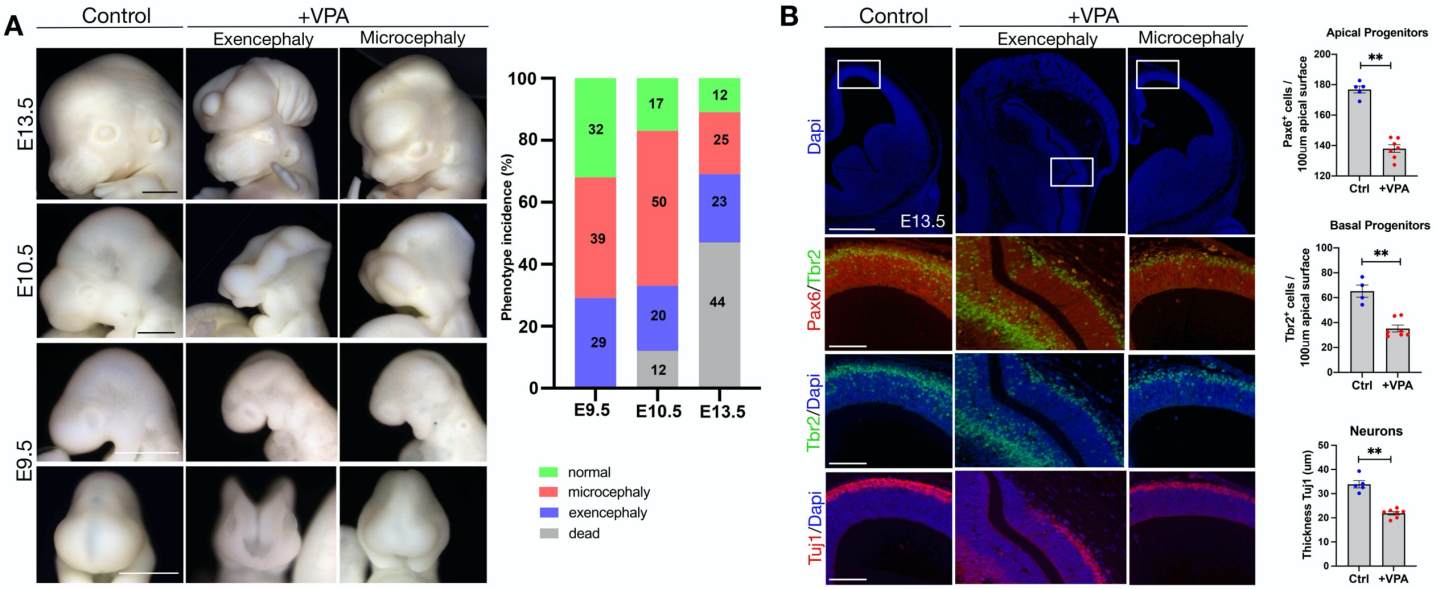


**Fig.1: Valproic acid treatment induces developmental defects, including exencephaly, microcephaly and corticogenesis impairment. (A)** Left: Embryonic head phenotypes in CD1 mice resulting from VPA exposure. Scale bar, 1mm (E13.5), 500µm (E9.5 and E10.5). Right: Phenotype incidence at different stages E9.5 (*n*= 147 embryos from 14 litters), E10.5 (*n*= 151 embryos from 16 litters) and E13.5 (*n*= 45 embryos from 4 litters). **(B)** Immunostaining for Pax6, Tbr2, Tuj1 on cortical sections (coronal) of E13.5 embryos. Box highlights the region in lower images. Scale bar, 500µm (top row), 100µm (rest). Quantification of Pax6 and Tbr2 positive progenitors or the thickness of the neuronal layer in the microcephalic cortical vesicles (for each condition, 5 embryos from at least 4 different mothers were analyzed). Data bars represent mean ± SEM. Mann-Whitney test: **p ≤ 0.01.

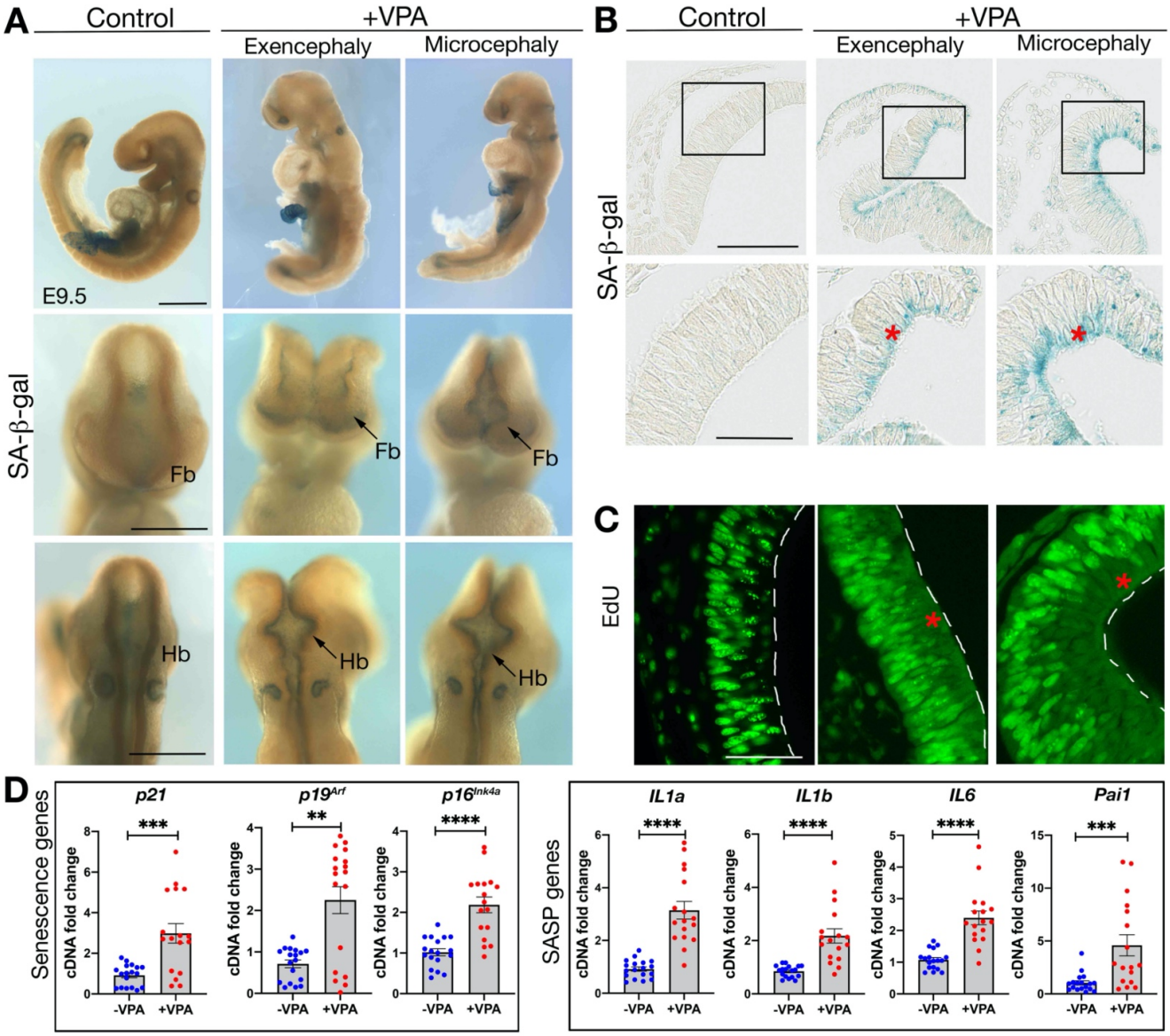


**Fig.2: Senescence is induced in the forebrain and hindbrain neuroepithelium of VPA-treated embryos. (A)** Whole mount SA-β-gal staining in control and VPA-treated embryos at E9.5 (*n*= 18 embryos from 7 litters). Top row, lateral views. Scale bar, 500μm. Middle row, frontal views and bottom row, dorsal views. Scale bars, 50μm. Fb, forebrain. Hb, Hindbrain. **(B)** Sections through whole mount SA-β-gal stained forebrains (Scale bar, 100μm). Box shows the region imaged in lower panel (scale bar, 50μm). Red asterisks highlight senescent cells. (*n*= 8 embryos from 4 litters). **(C)** EdU incorporation in neuroepithelial cells. Red asterisks indicate location of senescent cells (*n*= 6 embryos from 5 litters). White dashed lines indicate apical surface of the neural tube. EdU, 5-ethynyl-2′-deoxyuridine. Scale bar, 50 μm. **(D)** qRT-PCR analysis on E8.75 forebrain + midbrain, for senescence markers (*p21, p19$^{Arf}$, p16$^{Ink4a}$*) and SASP genes (*IL1a, IL1b, IL6* and *Pai1*) (*n*=17-18 embryos from 3 different litters). Data bars represent mean ± SEM. Mann-Whitney test: **p ≤ 0.01, ***p ≤ 0.001 and ****p ≤ 0.0001.

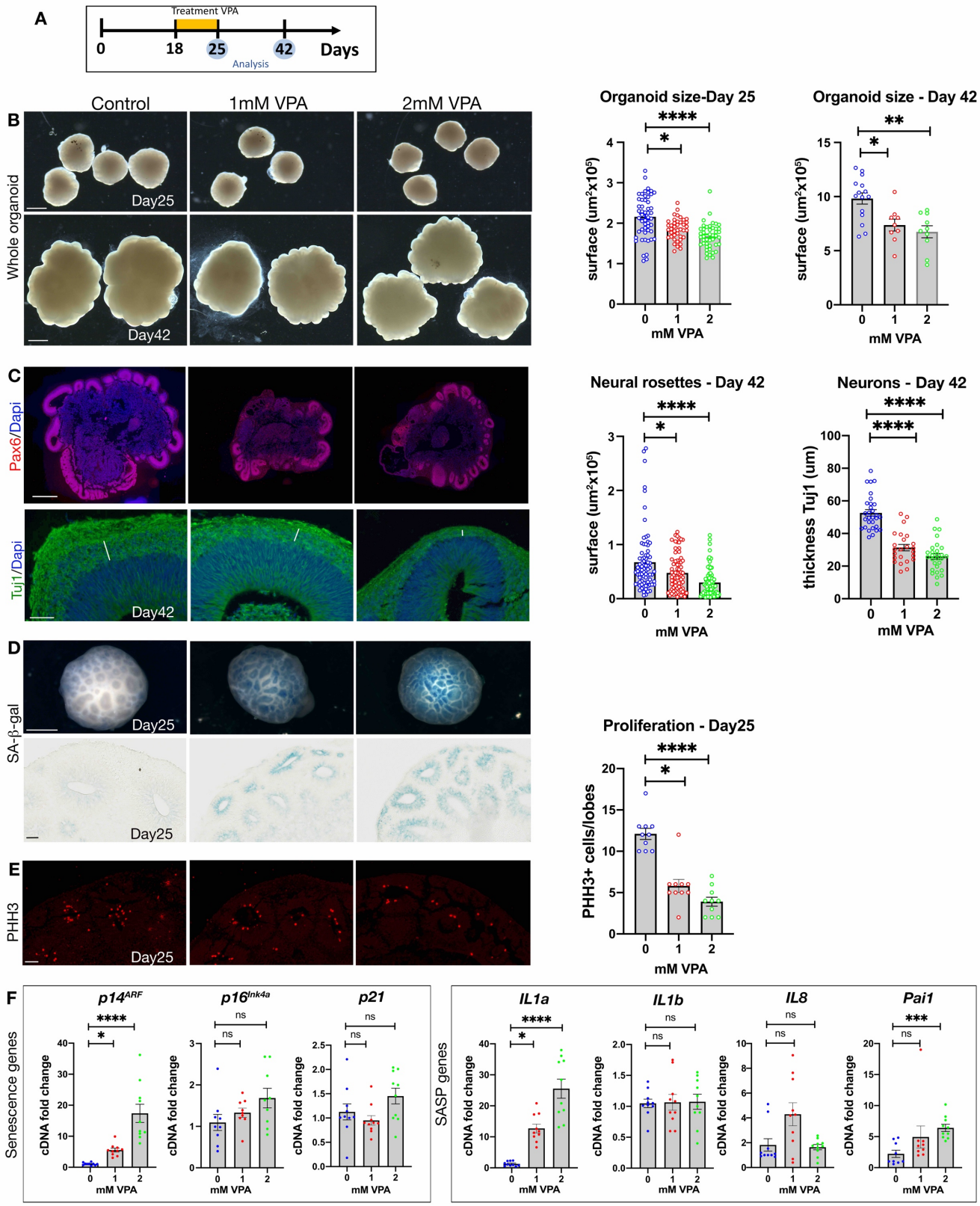


**Fig.3: Cerebral organoids treated with VPA show a decreased size, impaired neurogenesis and induction of senescence in neuroepithelial cells. (A)** Schematic for organoid cultures experiments. **(B)** Left: Bright field images of cerebral organoids at days 25 and day 42. Scale bar, 1 mm. Right: organoid size ($\mu m^2$) at day 25 ($n$ = 52 (Control), 41 (1mM VPA), 45 (2mM VPA), 4 independent experiments) and day 42 ($n$ = 15 (Control), 9 (1mM VPA), 10 (2mM VPA), 4 independent experiments). Data bars represent mean ± SEM. Kruskal-Wallis test: *p ≤ 0.05, **p ≤ 0.01 and ****p ≤ 0.0001. **(C)** Left: Immunostaining on sections of control

and VPA-treated organoids for Pax6 (red) or Tuj1 (green), counterstained with Dapi (blue). Scale bar, 500μm (Pax6) and 50μm (Tuj1). Right: Neural rosette area at day 42 (*n* = 79 (Control), 76 (1mM VPA), 79 (2mM VPA), 4 independent experiments), and neuron layer thickness (μm) at day 42 (*n* = 30 (Control), 24 (1mM VPA), 28 (2mM VPA), 4 independent experiments). Data bars represent mean ± SEM. Kruskal-Wallis test: *p ≤ 0.05, and ****p ≤ 0.0001. **(D)** Whole mount SA-β-gal staining of day 25 organoids (scale bar, 500μm). Sections show SA-β-gal staining in the neuroepithelium (scale bar, 50μm) (*n*= 5 (Control), 5 (1mM VPA), 5 (2mM VPA), 3 independent experiments). **(E)** Left: Immunostaining on sections of control and VPA-treated organoids for PHH3 (red) at day 25. Scale bar, 50μm. Right: Proliferation quantification at day 25. (n = 10 (Control), 10 (1mMVPA), 10 (2mMVPA), 2 independent experiments). Data bars represent mean ± SEM. Kruskal-Wallis test: *p ≤ 0.05 and ****p ≤ 0.0001. **(F)** qRT-PCR analysis for senescence markers (*p21, p14*$^{ARF}$*, p16*$^{INK4A}$) and for SASP genes (*IL1a, IL1b, IL8* and *Pai1*) (*n*=10 organoids from 4 independent experiments). Data bars represent mean ± SEM. Kruskal-Wallis test: ns, not significant, *p ≤ 0.05, ***p ≤ 0.001 and ****p ≤ 0.0001.

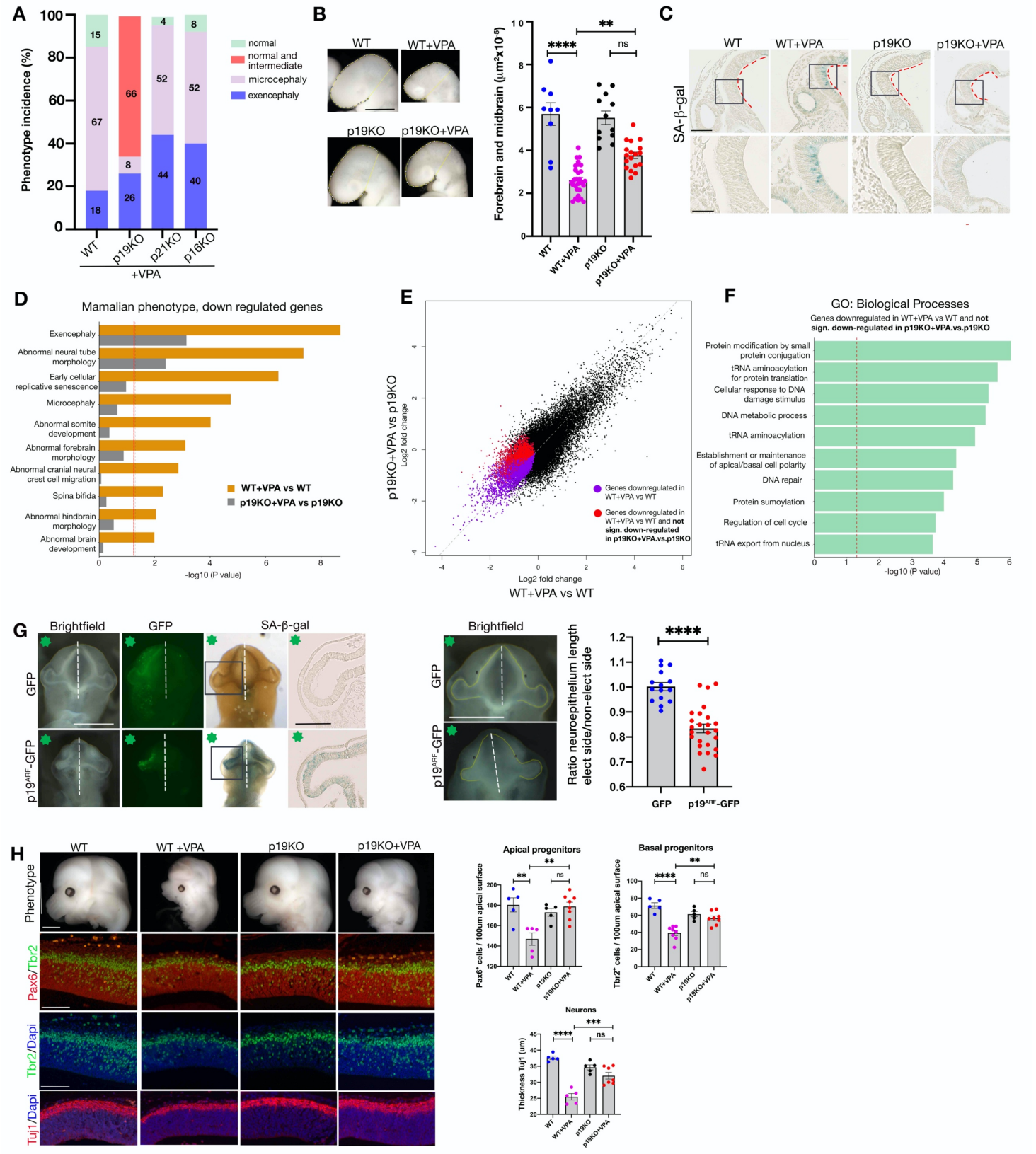


**Fig.4: *p19$^{Arf}$* deficiency rescues senescence and VPA-induced microcephaly**. **(A)** Phenotype incidence at E9.5 in C57/Bl6J mice. *p21*, *p19$^{Arf}$* or *p16$^{Ink4a}$* -deficient mice are labeled p21KO, p19KO or p16KO respectively. WT, *n*= 174 embryos from 26 litters. p19KO, *n*= 123 embryos from 19 litters, p21 KO, *n*= 72 embryos from 10 litters and p16KO, n= 97 embryos from 11 litters. **(B)** Bright field images of E9.5 embryonic heads, indicating area of the forebrain and midbrain (yellow line). Scale bar, 500µm. Graph shows surface area of

forebrain and midbrain in each condition, WT, *n*= 9 embryos from 4 litters, WT+VPA, *n*= 29 embryos from 14 litters, p19KO, *n*= 12 embryos from 4 litters, p19KO + VPA, *n*= 18 embryos from 7litters. Data bars represent mean ± SEM. Kruskal-Wallis test: ns, not significant, **p ≤ 0.01 and ****p ≤ 0.0001. **(C)** Representative brain sections of E9.5 SA-β-gal stained WT or p19KO (scale bar, 100μm). Box shows the region imaged in lower panel (scale bar, 50μm). Red dashed lines indicate apical surface of the neural tube. WT, *n*= 5 embryos from 3 litters, WT+VPA, *n*= 6 embryos from 4 litters, p19KO *n*= 5 embryos from 3 litters for p19KO, p19KO + VPA *n*= 9 embryos from 3litters. **(D)** Mammalian Phenotype pathway analysis on the downregulated genes from RNA-seq of the forebrain and midbrain **(E)** Scatter plot showing mRNA fold changes for the genes in WT+VPA compared to WT, and in p19KO + VPA compared to p19KO. **(F)** GO Biological process analysis on genes highlighted in E with red dot. **(G)** Ventral views of chick embryos at stage HH12, electroporated with a *GFP* or a $p19^{Arf}$-*GFP* plasmid. Green star indicates electroporated side. Scale bar, 500μm. Embryos were stained for SA-β-gal activity. Boxes indicate sectioned area of forebrain neuroepithelium shown. Scale bar, 100μm. Brightfield embryos with yellow line shows length of neuroepithelium. Scale bar, 500μm. Graph shows ratio of length of neuroepithelium in electroporated side compared to control side. GFP, *n* = 15 embryos from 4 different electroporations, $p19^{Arf}$-*GFP*, *n*= 25 embryos from 9 different electroporations. Data bars represent mean ± SEM. Unpaired t-test: ****p ≤ 0.0001. **(H)** Images showing the cortical vesicles. Scale bar, 1mm. Immunostaining on cortical sections, E.13.5, for Pax6, Tbr2, Tuj1 and counterstained with Dapi. Scale bar, 100μm. Graphs showing number of Pax6 and Tbr2 positive progenitors or the thickness of the Tuj1 neuronal layer in the cortical vesicles (for each condition, minimum 5 embryos from at least 4 different mothers were analyzed). Data bars represent mean ± SEM. One-way ANOVA plus Tukey post-hoc test: ns, no significant, **p ≤ 0.01, ***p ≤ 0.001 and ****p ≤ 0.0001.

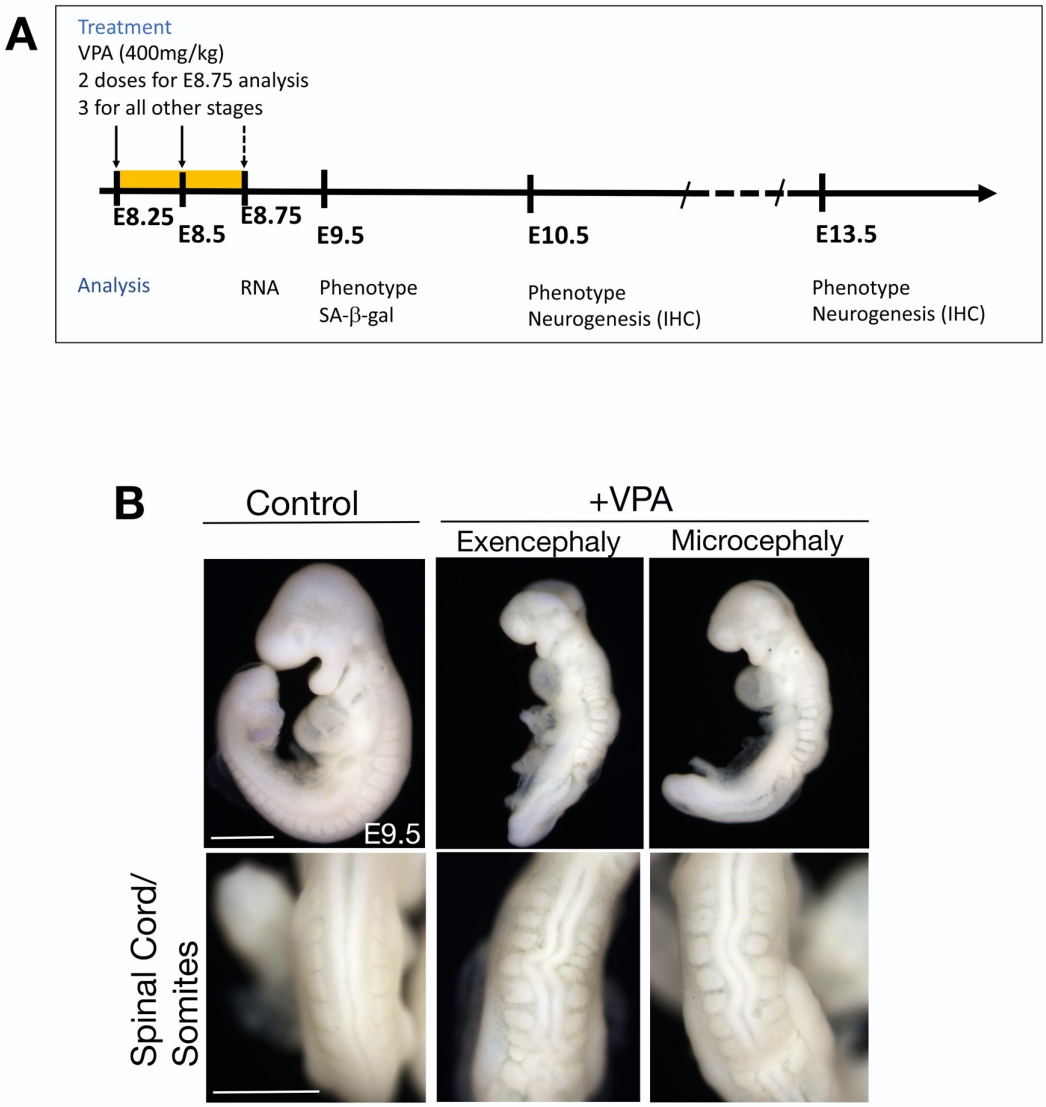


**Figure S1. VPA treatment leads to abnormal spinal cord and somite development.** **(A)** Schematic of experimental treatment of mice with VPA, and timeline of analysis. **(B)** Lateral views (top) and dorsal views (bottom) of control and VPA-treated embryos dissected at E9.5, illustrating the pronounced curve in the neural tube and abnormally shaped somites observed (*n*= 147 embryos from 14 litters). Scale bar, 500μm.

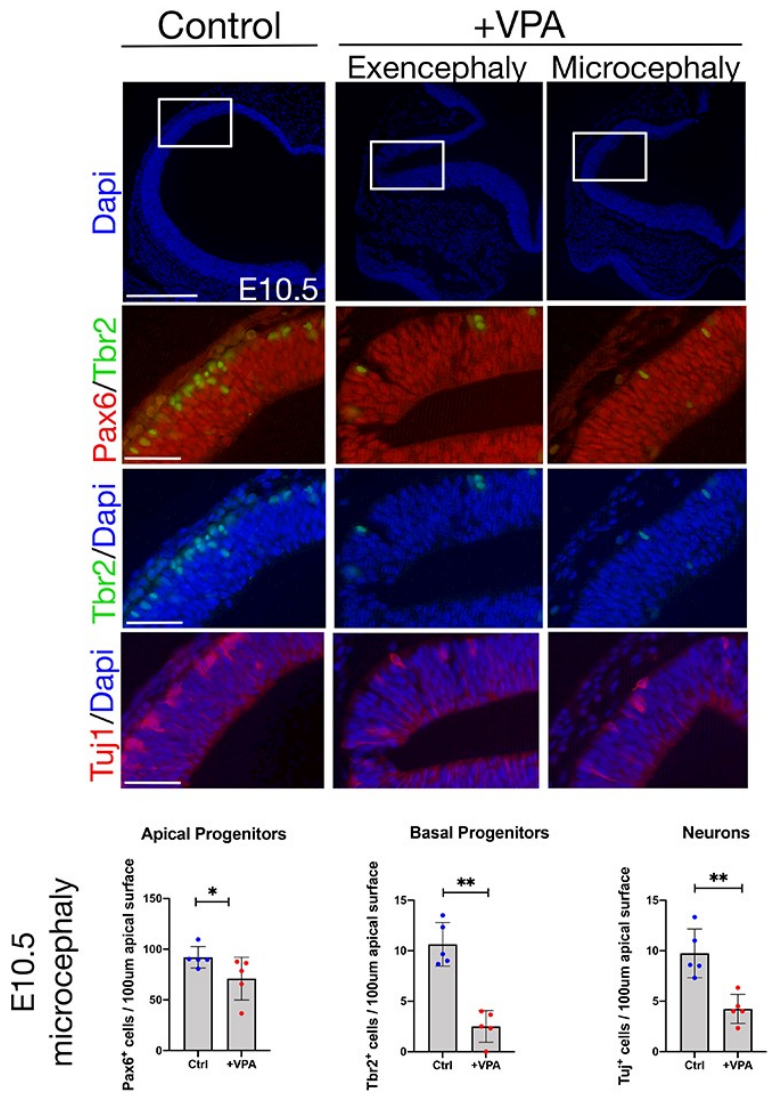


**Figure S2. Impaired neurogenesis after VPA treatment is already observed at E10.5.** Cortical sections (coronal) of E10.5 embryos were immunostained for Pax6, Tbr2, Tuj1 and counterstained with Dapi. Scale bar, 250μm (top row), 50μm. Graphs show quantification of Pax6 and Tbr2 positive progenitors or the thickness of the neuronal layer in the microcephalic cortical vesicles (5 embryos from at least 4 different mothers were analyzed). Data bars represent mean ± SEM Mann-Whitney test: *$p \leq 0.05$ and **$p \leq 0.01$.

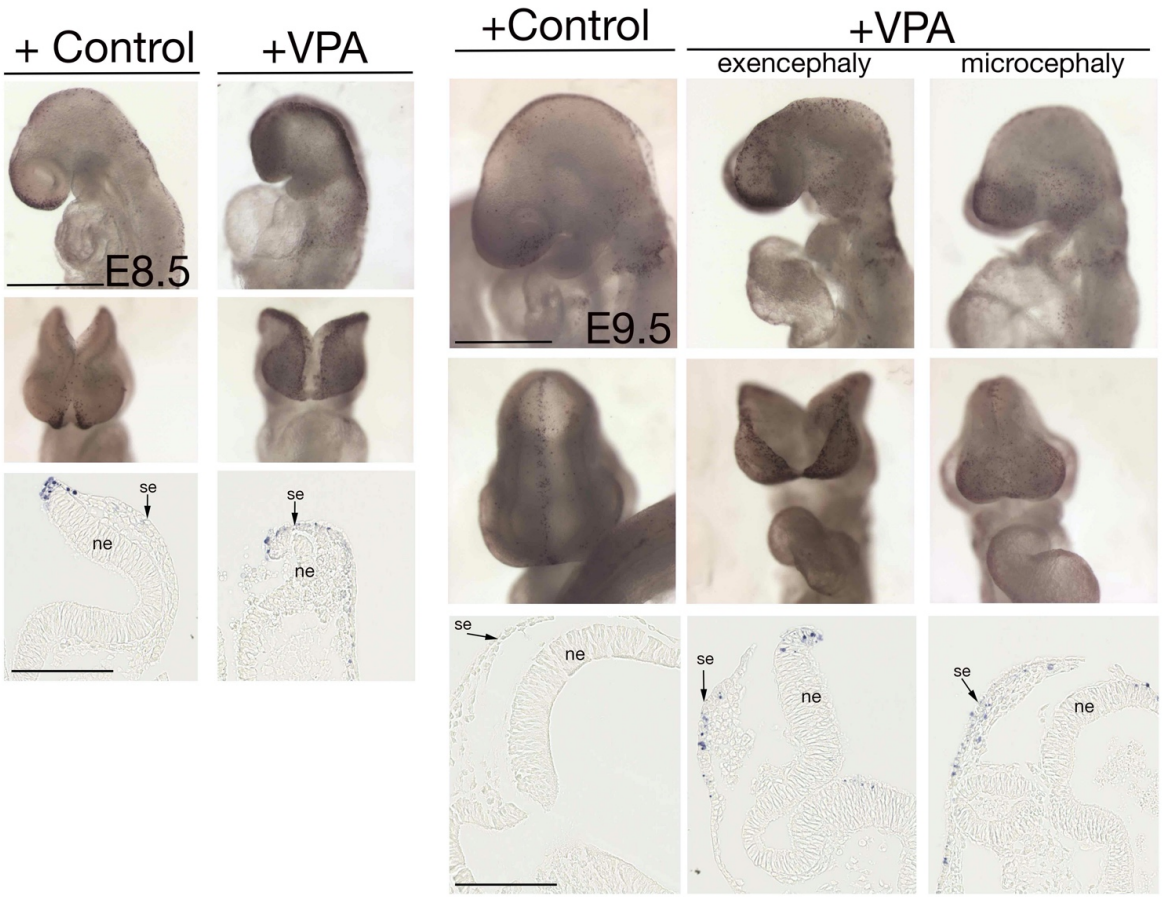


**Figure S3. VPA does not induce apoptosis in the forebrain neuroepithelium.** Control and VPA-treated embryos were stained with whole mount TUNEL assay, to assess cell death. (Left) Lateral views and frontal views of control and VPA-treated embryos dissected at E8.5. Scale bar, 500μm. Corresponding horizontal sections at the forebrain level (3 embryos from at least 2 litters were analyzed). Scale bar, 100μm. (Right) Lateral views and frontal views of control and VPA-treated embryos dissected at E9.5 (6 embryos from at least 5 litters were analyzed). Scale bar, 500μm. Corresponding horizontal sections at the forebrain level. Scale bar, 100μm. Some apoptotic cells are observed in the surface ectoderm. ne = neuroepithelium, se = surface ectoderm.

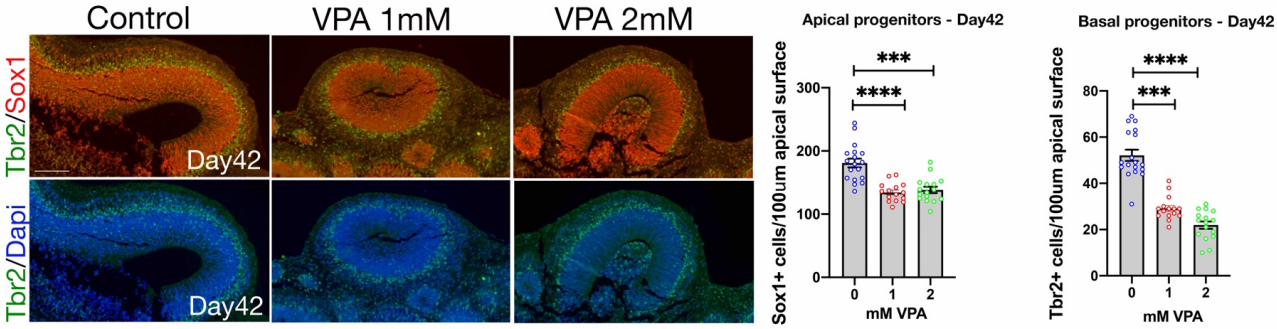


**Figure S4. Neurogenesis is impaired in cerebral organoids treated with VPA.** Sections through control and VPA-treated organoids were immunostained with Sox1(red), Tbr2 (green) and Dapi (blue) at day 42 (Scale bar, 50μm), (*n* = 15 (Control), 12 (1mM VPA), 13 (2mM VPA), 4 independent experiments). Kruskal-Wallis test: ****p ≤ 0.001 and ****p ≤ 0.0001.

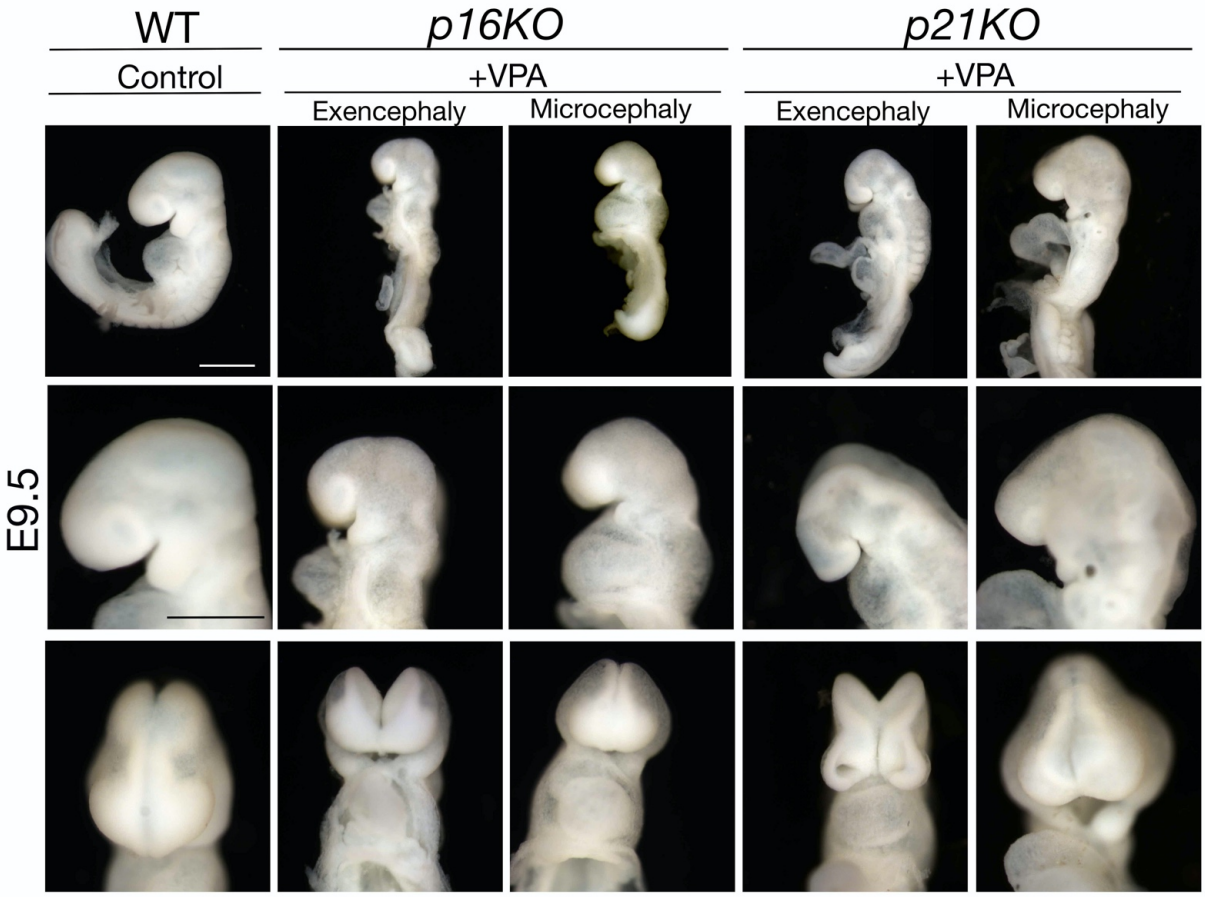


**Figure S5. Genetic deficiency of *p16$^{Ink4a}$* or *p21* does not rescue VPA induced phenotypes.** Lateral views of control and VPA-treated embryos deficient for *p16$^{Ink4a}$* or *p21* (top row). Scale bar, 500μm. Higher magnification of the heads in lateral (middle row) and frontal views (bottom row). Scale bar, 50μm. An open neural tube or a smaller brain, as well as a gross misalignment of the neural tube and somites are still observed after VPA treatment in the absence of *p16$^{Ink4a}$* or *p21*.

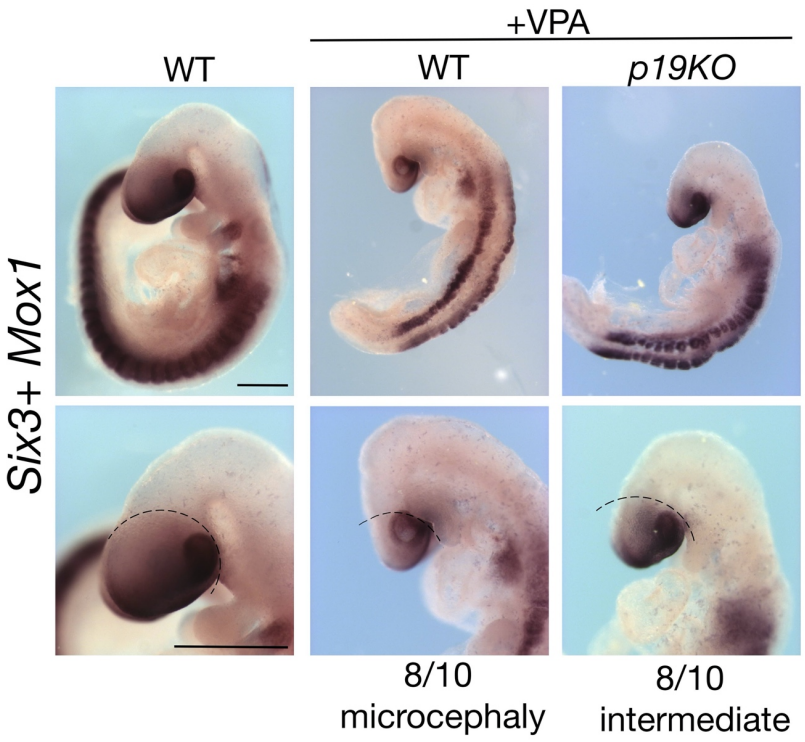


**Figure S6. Improved forebrain phenotype in *p19$^{Arf}$* deficient mice after VPA treatment.** Whole mount *in situ* hybridization for *Six3* (forebrain) and *Mox1* (somites), showing an increased size of the forebrain in *p19$^{Arf}$*-deficient, VPA-treated mice in comparison to the *WT* mice treated with VPA. Scale bar, 500μm (top row) and 50μm (bottom row). The number of embryos examined are indicated (*n*=10 from at least 5 different litters).

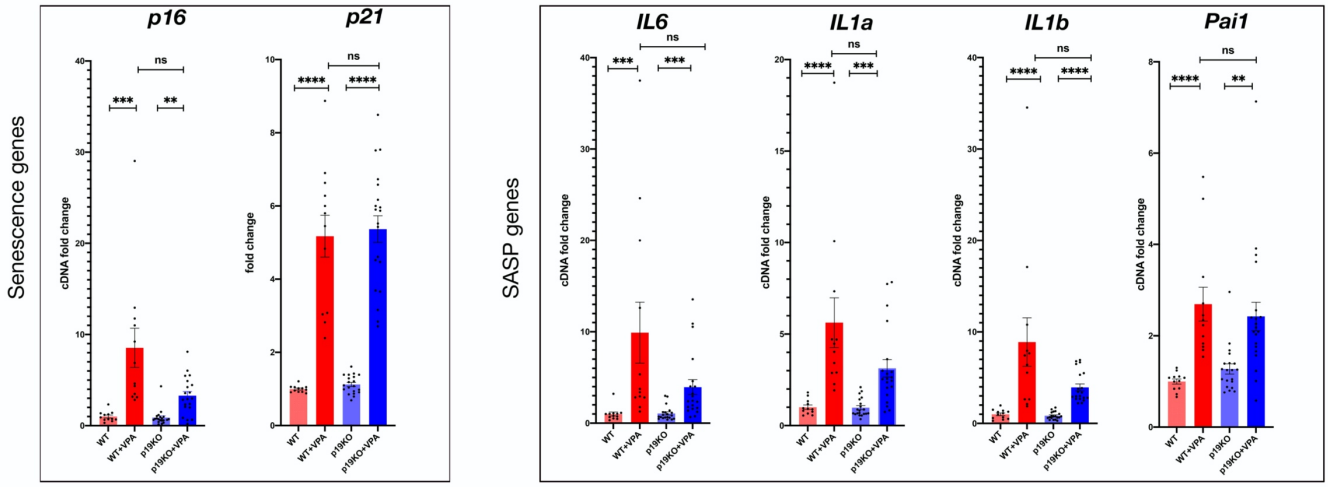


**Figure S7. Senescence and SASP genes are less induced in *p19$^{Arf}$*-deficient embryos with VPA treatment.** qRT-PCR analysis on E8.75 forebrain and midbrain, from control and *p19$^{Arf}$*-deficient mice, treated with VPA or left untreated. Graphs show fold change expression for the senescence markers (*p21, p16$^{Ink4a}$*) and for SASP genes (*IL6, IL1a, IL1b,* and *Pai1*), normalized to untreated control ($n$ = 12 (Control), $n$=12 (Control+VPA), $n$=20 (*p19KO*), $n$=20 (*p19KO*+VPA), from at least 3 different litters). Data bars represent mean ± SEM. Kruskal-Wallis test: ns, no significant, **p ≤ 0.01, ***p ≤ 0.001 and ****p ≤ 0.0001.

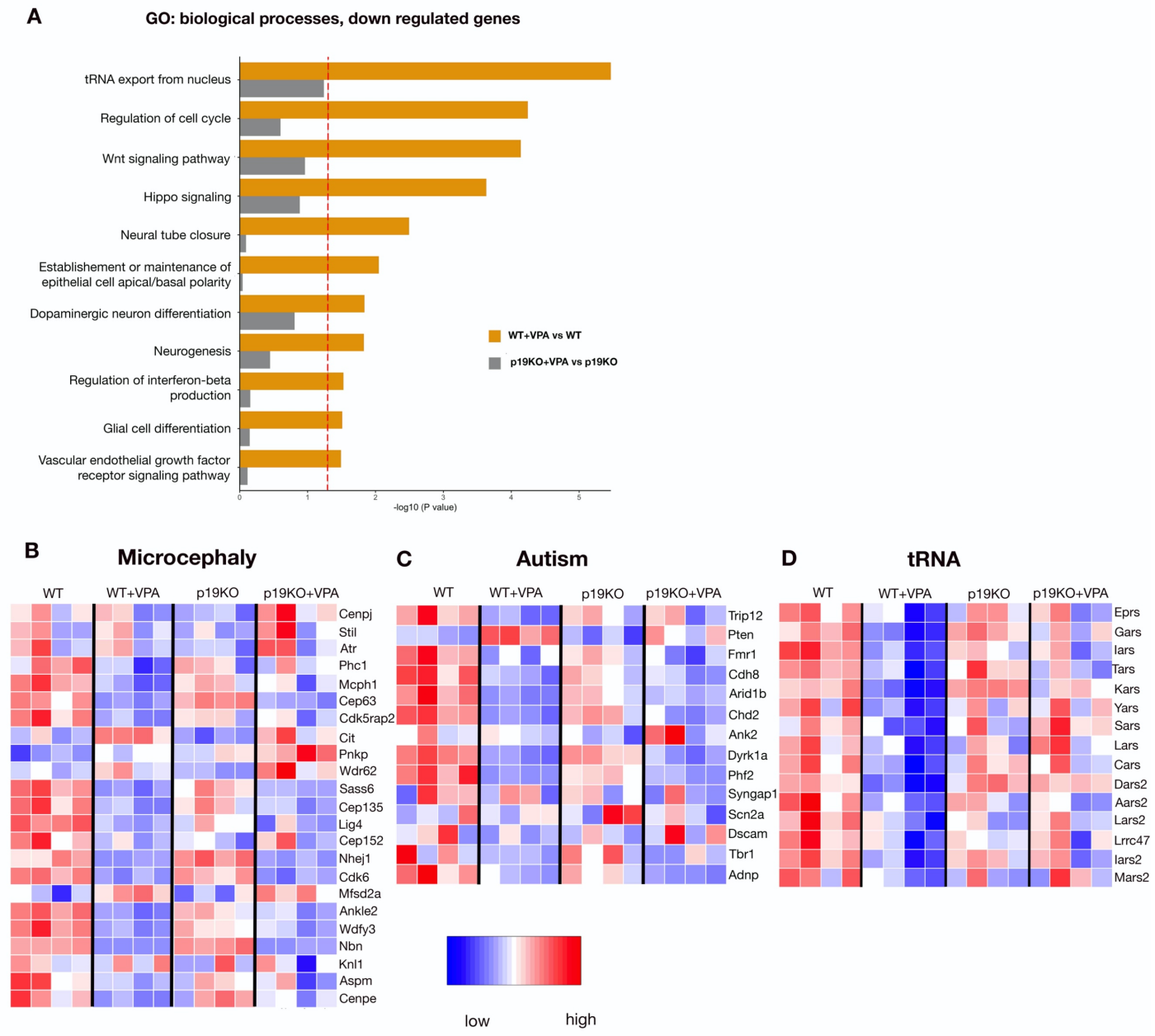


**Figure S8. RNA-sequencing data analysis uncovers neurodevelopmental and tRNA related signatures as being less affected by VPA treatment in *p19$^{Arf}$*-deficient mice. (A)** GO Biological Processes pathway analysis on the downregulated genes from RNA-seq of the forebrain and midbrain **(B)** Heat Maps showing the relative expression of representative genes associated with Microcephaly (list generated from Jayaraman et al, 2018), Autism (List generated from Jayaraman et al, 2018) and tRNA (list of genes identified in Fig 4F pathway analysis).

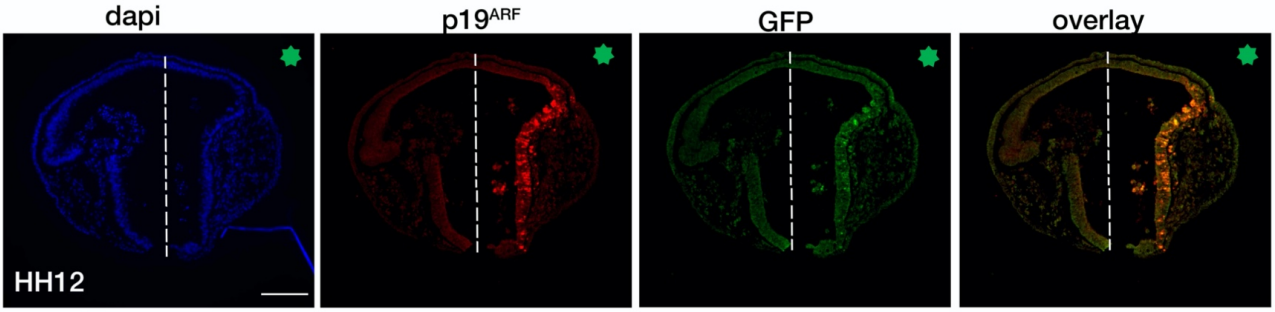


**Figure S9. Ectopic expression of *p19$^{Arf}$-GFP* in the chicken neural tube.** Sections through the neural tube of *p19$^{Arf}$-GFP* electroporated chicken embryos electroporated at stage HH12, immunostained for p19$^{Arf}$ (red) and GFP (green), with Dapi counterstaining (blue). The green star shows the electroporated side. Scale bar, 100μm.

***Supplementary Table 1***

| **Human primers** | **Sequence** |
|---|---|
| GAPDH-fwd | AAGGTGAAGGTCGGAGTCAAC |
| GAPDH-rev | GGGGTCATTGATGGCAACAATA |
| $p14^{ARF}$ -fwd | CTGATGCTACTGAGGAGCCA |
| $p14^{ARF}$ -rev | TCATGACCTGGTCTTCTAGG |
| p16INK4A-fwd | GGTCGGAGGCCGATCCAGGTCA |
| p16INK4A-rev | TTCAATCGGGGATGTCTGAGG |
| p21-fwd | CGAAGTCAGTTCCTTGTGGAG |
| p21-rev | CATGGGTTCTGACGGACAT |
| IL1a-fwd | ACTGCCCAAGATGAAGACCAA |
| IL1a-rev | CCGTGAGTTTCCCAGAAGAAGA |
| IL1b-fwd | TTCGACACATGGGATAACGAGG |
| IL1b-rev | TTTTTGCTGTGAGTCCCGGAG |
| IL8-fwd | ACTGAGAGTGATTGAGAGTGGAC |
| IL8-rev | AACCCTCTGCACCCAGTTTTC |
| PAI1-fwd | AAGATCGAGGTGAACGAGAGTG |
| PAI1-rev | GACCACAAAGAGGAAGGGTCT |
| | |
| **Mouse primers** | **Sequence** |
| Rplp0 | QT00249375(QIAGEN) |
| $P19^{Arf}$ | QT01164891 (QIAGEN) |
| $p16^{Ink4a}$ | QT01164898(QIAGEN) |
| p21 | QT00137053(QIAGEN) |
| Il1a-fwd | GCACCTTACACCTACCAGAGT |
| Il1a-rev | AAACTTCTGCCTGACGAGCTT |
| Il1b-fwd | TTCAGGCAGGCAGTATCACTC |
| Il1b-rev | GAAGGTCCACGGGAAAGACAC |
| Il6-fwd | TAGTCCTTCCTACCCCAATTTCC |
| Il6-rev | TTGGTCCTTAGCCACTCCTTC |
| Pai1-fwd | TGGGTGGAAAGGCATACCAAA |
| Pai1-rev | AAGTAGAGGGCATTCACCAGC |
| MMP9-fwd | GCGTCATTCGCGTGGATAAG |
| MMP9-rev | TGGAAACTCACACGCCAGAA |

**Table S1. Primers used for qRT-PCR in the study.** The table lists the primer sequences or source for both human and mouse genes used in the study.